### Title
Calculating Trajectories Associated With Solute Transport in a Heterogeneous Medium




### Journal
Water Resources Research, 54(9)

### ISSN
0043-1397



### Authors
Vasco, DW
Pride, Steven R
Zahasky, Christopher
et al.



### Publication Date
2018-09-01

### DOI
10.1029/2018wr023019

Peer reviewed

# Calculating Trajectories Associated With Solute Transport in a Heterogeneous Medium

D. W. Vasco[1], Steven R. Pride[1], Christopher Zahasky[2], and Sally M. Benson[2]

[1]Energy Geosciences Division, Lawrence Berkeley National Laboratory, Berkeley, CA, USA, [2]Department of Energy Resources Engineering, Stanford University, Stanford, CA, USA

Correspondence to: D. W. Vasco, dwvasco@lbl.gov

## Abstract

We present a trajectory-based technique for calculating solute transport in a porous medium that has several advantages over existing methods. Unlike streamlines, the extended trajectories are influenced by each of the important parameters governing transport, including molecular diffusion and transverse dispersion. The approach is complete and does not require any additional techniques, such as operator splitting or particle tracking, in order to account for the full dispersion tensor. The semianalytic expressions make it clear how the flow field, the concentration distribution, and the dispersion tensor contribute to the velocity field of an injected solute. The equations are valid for an arbitrary porous medium, including those with rapid spatial variations in properties, overcoming limitations faced by previous approaches based upon asymptotic techniques. A test on a layered model with sharp boundaries indicates that the extended trajectories are compatible with the results of a numerical simulator and differ from streamlines. We also describe a new form of the dispersion tensor that incorporates a known asymmetry. The trajectories indicate that the modifications of the dispersion tensor lead to more focused transport within regions of high conductivity. Finally, the trajectories are used to define a semianalytic relationship between solute travel times and variations in solute velocities along a path that may be used for tomographic imaging. In an application to the injection of a radioactive tracer into a Berea sandstone core, monitored using micropositron emission tomographic (micro-PET) observations, the sensitivities are used to map the spatial variations of permeability within the core.

## 1 Introduction

Solute transport is an important aspect of hydrology and a useful aid in understanding fluid flow and in reservoir characterization. The transportation of dissolved substances is critical for activities such as groundwater remediation, enhanced oil recovery, and agriculture. Advanced techniques, such as the use of arrays of multilevel samplers and partitioning tracers (Datta-Gupta et al., 2002) have extended the usefulness of transport data for reservoir characterization and the mapping of fluid saturations in three dimensions. The incorporation of geophysical techniques for monitoring tracer transport have proven valuable in imaging two- and three-dimensional solute migration as a function of time. For example, electrical resistance

tomography (ERT) has been used to track the migration of a saline plume within a groundwater system (Doetsch et al., 2012) and to image infiltrating river water (Coscia et al., 2012). Crosswell and surface ground-penetrating radar (GPR) have been used to image saline fluid movement along fractures in the subsurface (Becker & Tsoflias, 2010; Day-Lewis et al., 2003; Tsoflias & Becker, 2008).

The movement of a solute is a complicated process that depends upon the spatial variations in flow properties over several scales. First, there is a dependence upon the flow field that is controlled by medium- and large-scale spatial variations in permeability. Second, transport depends upon small-scale or local flow that determines the nature of the dispersion of the solute, such as its anisotropy (Dagan, 1982, 1987; Gelhar et al., 1979; Gelhar & Axness, 1983; Schwartz, 1977). The variability in geological porous media, where there may be significant deviations in grain distributions and sizes and fracture density, is an additional complicating factor. As a result of these issues, the nature of the dispersion tensor is an area of active research (Auriault et al., 2010; Delgado, 2007; Flekkoy et al., 2017; Lichtner et al., 2002; Liu & Kitanidis, 2013; Pride et al., 2017).

Because of the complexity of solute transport, it is a challenge to accurately model the process. Analytic approaches are generally restricted to simplified structures such as a homogeneous whole space, a semiinfinite half-space, or a uniform layer (Javandel et al., 1984; Park & Zhan, 2001; van Genuchten & Alves, 1982). Methods based upon integral transforms produce semianalytic solutions that are valid in general layered and one-dimensional porous media (Guerrero & Skaggs, 2010; Moridis, 2002; Shan & Javandel, 1997; Yates, 1990). The most straightforward numerical techniques, Eulerian approaches on fixed numerical grids, are very general (Oldenburg & Pruess, 1995, 1996) but typically suffer from numerical dispersion and unstable oscillations in the presence of sharp concentration fronts necessitating small time steps or more sophisticated differencing schemes (Crane & Blunt, 1999; Datta-Gupta et al., 1991; Oldenburg & Pruess, 1998). Lagrangian methods, whereby one tracks the movement of solute particles in a calculated flow field, have proven successful in modeling advective transport with little or no dispersion. Lagrangian methods may be broadly classified as particle tracking techniques (Bear & Verruijt, 1987; Zheng & Bennett, 1995), stream function calculations (Fogg & Senger, 1985; Javandel et al., 1984; Nelson, 1978), and streamline methods (Crane & Blunt, 1999; Datta-Gupta & King, 1995, 2007).

If dispersion is significant, the Lagrangian approaches must be modified, using such techniques as the random walk model (Prickett et al., 1981), operator splitting (Bratvedt et al., 1996), smoothed particle hydrodynamics (Herrera et al., 2009, 2010; Tartakovsky et al., 2008), or stochastic streamline methods(Cirpka et al., 2011; Dagan & Cvetkovic, 1996) to model lateral and transverse dispersion. A hybrid mixed Eulerian-Lagrangian method, known as the method of characteristics (Konikow & Bredehoft,

1978), combines particle tracking and Eulerian numerical methods by averaging the concentration of particles within the cells of the fixed grid. Asymptotic techniques (Chapman et al., 1999; Smith, 1981; Vasco & Finsterle, 2004; Vasco et al., 2016) provide an alternative, grid-free means for modeling transport, though the approach is restricted to porous media with smoothly varying properties.

In this paper we present a trajectory-based technique for calculating solute transport. The trajectories are influenced by the diffusive and dispersive properties of the medium, similar to the asymptotic paths developed in Vasco et al. (2016). Moreover, the paths presented below are valid for an arbitrary porous medium and rapid spatial variations in medium properties are not an issue, as long as the macroscopic heterogeneity is several times larger than the representative elementary volume used to average over microscopic variations in properties (de Marsily, 1986, p. 15). The approach allows for a general dispersion tensor and a time-varying flow field. We shall discuss some modifications of the dispersion tensor that provide a form compatible with the results of Koch and Brady (1987), Auriault et al. (2010), and Pride et al. (2017). The expression for the trajectories provides a means for computing a semianalytic sensitivity relating a tracer arrival time to variations in hydraulic conductivity along the trajectory. Such sensitivities form the basis for a tomographic imaging algorithm. We illustrate this imaging technique through an application to positron emission tomographic (PET) monitoring of the injection of a radiotracer into a core of Berea sandstone.

## 2 Methodology

### 2.1 Trajectories Associated With Solute Transport

The equation governing the evolution of a solute concentration $c(\mathbf{x},t)$ in a velocity field $\mathbf{q}(\mathbf{x},t)$ is

$$\nabla \cdot (\mathbf{D} \cdot \nabla c - \mathbf{q}c) = \varphi \frac{\partial c}{\partial t} \quad \text{(1a)}$$

where

$$\mathbf{q} = -\frac{k}{\mu} \nabla p, \quad \text{(1b)}$$

$\mathbf{D}(\mathbf{x},t)$ is the dispersion tensor, $\varphi(\mathbf{x})$ is the kinematic porosity, $k(\mathbf{x})$ is the specific permeability, $\mu$ is the fluid viscosity, and $p(\mathbf{x},t)$ is the fluid pressure. The kinematic porosity is the accessible pore space, that is, the pores that may be visited by solute particles carried along in the flow field $\mathbf{q}$. We discuss the dispersion tensor in greater detail in Appendix A. The effects of density differences between the solute and the aqueous fluid are assumed to be negligible in equations 1a and 1b.

A trajectory-based solution for the evolution of the solute follows from a representation of the concentration in an exponential form

$$c(\mathbf{x}, t) = e^{-S(\mathbf{x},t)}. \quad (2)$$

Substituting this form into the governing equation 1a produces

$$\varphi \frac{\partial S}{\partial t} + \mathbf{q} \cdot \nabla S + \nabla S \cdot \mathbf{D} \cdot \nabla S = \nabla \cdot (\mathbf{q} + \mathbf{D} \cdot \nabla S) \quad (3)$$

a nonlinear partial differential equation for $S(\mathbf{x},t)$. Defining the vectors

$$\mathbf{p} = \nabla S, \quad (4)$$

$$\mathbf{v} = \frac{1}{\varphi} (\mathbf{q} + \mathbf{p} \cdot \mathbf{D}), \quad (5)$$

and

$$\mathbf{w} = \mathbf{q} + \mathbf{D} \cdot \mathbf{p} \quad (6)$$

one can write equation 3 as

$$\frac{\partial S}{\partial t} + \mathbf{v} \cdot \nabla S = \frac{1}{\varphi} \nabla \cdot \mathbf{w}. \quad (7)$$

The form of equation 7 suggests a Lagrangian reference frame moving with velocity **v**. For such a reference frame we may consider a path $\mathbf{x}(t)$ and a total derivative of $S(\mathbf{x},t)$ along that path,

$$\frac{\mathrm{d}S}{\mathrm{d}t} = \frac{\partial S}{\partial t} + \mathbf{v} \cdot \nabla S = \frac{\partial S}{\partial t} + \frac{\mathrm{d}\mathbf{x}}{\mathrm{d}t} \cdot \nabla S, \quad (8)$$

where the trajectory $\mathbf{x}(t)$ is defined by

$$\frac{\mathrm{d}\mathbf{x}}{\mathrm{d}t} = \mathbf{v} = \frac{1}{\varphi} (\mathbf{q} + \mathbf{p} \cdot \mathbf{D}). \quad (19)$$

Due to the presence of the unknown vector **p**, equation 19 is not sufficient to determine the path. To produce an equation for **p**, we return to equation 7, representing the left-hand side by the total derivative of $S(\mathbf{x},t)$ and using 6 to define **w** in terms of **D**, **p** and **q**

$$\frac{\mathrm{d}S}{\mathrm{d}t} = \frac{1}{\varphi} \nabla \cdot (\mathbf{q} + \mathbf{D} \cdot \mathbf{p}). \quad (10)$$

Applying the gradient operator ∇ to both sides of equation 10 and using the definition of **p** in equation 4 produces the other differential equation

$$\frac{\mathrm{d}\mathbf{p}}{\mathrm{d}t} = \nabla \left[ \frac{1}{\varphi} \nabla \cdot (\mathbf{q} + \mathbf{D} \cdot \mathbf{p}) \right] \quad (11)$$

and completes the system of equations determining **x** and **p**.

Summarizing the preceding developments, the system of equations

$$\frac{\mathrm{d}\mathbf{x}}{\mathrm{d}t} = \frac{1}{\varphi} (\mathbf{q} + \mathbf{p} \cdot \mathbf{D}) \quad (12)$$

$$\frac{\mathrm{d}\mathbf{p}}{\mathrm{d}t} = \nabla \left[ \frac{1}{\varphi} \nabla \cdot (\mathbf{q} + \mathbf{D} \cdot \mathbf{p}) \right] \quad (13)$$

defines the trajectory $\mathbf{x}(t)$ and the gradient vector $\mathbf{p}(t)$ along the trajectory. The differential equation 10 provides the final expression for $S(\mathbf{x}(t), t) = -\log c(\mathbf{x}, t)$ along the trajectory. From equation 12 it is clear that the trajectories depend upon the dispersion matrix **D**, the kinematic porosity $\varphi$,

and the flow field **q**. Given suitable initial and boundary conditions, one can solve this coupled system of ordinary differential equations using established numerical techniques (Cash & Carp, 1990; Press et al., 1999). Such an approach is used in quantum mechanics to solve a similar system of equations associated with Schrödinger's equation for chemical systems (Goldfarb et al., 2006; Garashchuk, 2010; Garashchuk & Vazhappilly, 2010; Garashchuk et al., 2011; Liu & Makri, 2006; Wyatt, 2005). However, the presence of the gradient operators in equation 13 complicates the numerical treatment by introducing nonlocal effects and coupling the calculations for neighboring trajectories. For example, one may extend the numerical methods, for instance, by computing the trajectories simultaneously and interpolating quantities onto a background numerical mesh (Wyatt, 2005). Such approaches are quite efficient and faster than a finite difference solution of the full Schrödinger's equation, particularly for complex chemical systems (Bittner et al., 2010; Gu & Garashchuk, 2016).

## 2.2 Relationship to Existing Techniques

Streamline simulation is an efficient approach for modeling transport processes (Crane & Blunt, 1999; Datta-Gupta & King, 1995, 2007; Fay & Pratts, 1951; Hewett & Behrens, 1991; Higgins & Leighton, 1962; Strack, 1984; Yabusaki et al., 1998). In streamline simulation the trajectories used in the modeling of solute transport are determined by the flow field q

$$\frac{\mathrm{d}\mathbf{x}}{\mathrm{d}t} = -\frac{\mathbf{q}}{\varphi}, \quad (14)$$

and the solute concentrations are found by solving a series of one-dimensional conservation equations defined along each streamline (Datta-Gupta & King, 2007). Streamline simulation is most accurate for advection-dominated transport and typically does not account for dispersion. As mentioned in section 1, cross-streamline mechanisms can be incorporated by a technique such as operator splitting (Bratvedt et al., 1996; Datta-Gupta & King, 2007; Obi & Blunt, 2004; Vasco & Datta-Gupta, 2016), smoothed particle hydrodynamics (Herrera et al., 2009, 2010; Tartakovsky et al., 2008), or stochastic streamline methods (Cirpka et al., 2011; Dagan & Cvetkovic, 1996). It is evident in equation 14 that streamlines follow the flow field and are not influenced by the dispersion tensor **D**. Comparing equations 12 and 14, we can interpret the trajectories in our approach as an extension of streamline modeling that includes the dispersion tensor in defining the path $\mathbf{x}(t)$. The sign difference between equation 14 and the first term on the right-hand side of equation 12 is due to the fact that we used the definition 2 with a negative sign for the exponent. Thus, $\nabla c = -\nabla S e^{-S}$ and hence $\mathbf{p} = \nabla S$ points in the opposite direction to the concentration gradient, and the path is traversed in the opposite direction.

Asymptotic techniques provide semianalytic, trajectory-based solutions to convection-diffusion equations such as 1a. Such methods are restrictive in the sense that they assume that some coefficient or parameter, such as

frequency, attains large or small values (Chapman et al., 1999; Knessl & Keller, 1997; Smith, 1981) or that the properties of the medium are smoothly varying in comparison to the length scale of the propagating tracer front (Vasco & Finsterle, 2004). The analysis of Vasco et al. (2016) produced a set of ordinary differential equations, the characteristic equations

$$\frac{d\mathbf{x}}{dt} = -\frac{1}{\varphi}\left(\mathbf{q} - 2\mathbf{D}\cdot\mathbf{p}\right) \quad (15)$$

$$\frac{d\mathbf{p}}{dt} = \left[\nabla\left(\frac{\mathbf{q}}{\varphi}\right) - \mathbf{p}\cdot\nabla\left(\frac{\mathbf{D}}{\varphi}\right)\right]\cdot\mathbf{p}, \quad (16)$$

for the path $\mathbf{x}(t)$ and gradient vector $\mathbf{p}(t)$. These equations, valid for a medium with smoothly varying properties, are generalizations of those given by Smith (1981) and Chapman et al. (1999) that allow for spatial variations in the medium properties and a full dispersion tensor. Equations 15 and 16 may be solved using numerical techniques for integrating systems of ordinary differential equations (Cash & Carp, 1990; Press et al., 1999). These two equations are somewhat similar to the extended equations 12 and 13, with a few important differences. First, only first-order derivatives appear in equation 16 while equation 13 contains second derivatives. Second, the derivatives in equation 16 are projected onto the vector **p,** while the expression on the right-hand side of equation 13 may contain contributions that are not in the direction of the vector **p**. Finally, equations 15 and 16 are only valid when the heterogeneity is smoothly varying in comparison to the length scale of the tracer front (Vasco et al., 2016). That is, the heterogeneity must vary smoothly in comparison to the width of the transition zone from the background solute concentration to the concentration behind the tracer front. In essence, the asymptotic approach is equivalent to neglecting the right-hand side in equation 3. If the medium, flow field, and concentration distribution are smoothly varying, then the divergence of the term on the right-hand side may be neglected and an eikonal equation results (Vasco & Datta-Gupta, 2016; Vasco et al., 2016). The characteristic equations associated with the eikonal equation are given by 15 and 16.

## 2.3 A Physical Interpretation of the Velocity Vector

By considering end member solutions, such as when the background concentration or the flow field vanishes, we gain insight into the two primary contributions to the velocity vector **v**, defined by equation 5. First, we use equation 2 to determine $S(\mathbf{x},t)$ in regions where the concentration does not vanish

$$S(\mathbf{x},t) = -\ln c(\mathbf{x},t). \quad (17)$$

Equation 17 provides values of $\mathbf{p}(\mathbf{x}(t),t)=\nabla S$ along the trajectory. Substituting this into equation 5 provides an expression defining the velocity vector along the trajectory

$$\frac{d\mathbf{x}}{dt} = \mathbf{v} = \frac{1}{\varphi}\left(\mathbf{q} - \nabla \ln c\cdot\mathbf{D}\right). \quad (18)$$

Now consider the case in which the concentration gradient is zero or there is no diffusion or dispersion so that **D** vanishes. In this case the velocity vector **v** is the Darcy flow velocity and the trajectory is identical to a streamline, given by equation 14. Alternatively, if the flow field **q** vanishes, then the only contribution comes from the second term on the right-hand side of equation 18. Substituting the standard form of the dispersion tensor, given in Appendix A by equations A5 and A6, into equation 18 and setting **q** to zero gives

$$\frac{\mathrm{d}\mathbf{x}}{\mathrm{d}t} = \mathbf{v} = -\frac{d_m}{F}\nabla \ln c$$

where $d_m$ is the molecular diffusion and $F$ is the formation factor (de Marsily, 1986, p. 34), and the velocity vector, and hence the path, follows the gradient of $\ln c(\mathbf{x}, t)$ . In this case molecular diffusion controls the movement of the solute, and hence, the paths are determined by the distribution of the solute. The velocity vector is usually a combination of these two scenarios in which both the flow field and the concentration-dependent diffusion and dispersion influence the solute movement. The vector **p** is a measure of the deviation from purely advective transport. That is, the degree to which the advected component dominates the concentration-dependent component depends upon the relative magnitude of the vectors **q** and **p** and on the dispersion of the medium, as determined by the tensor **D**.

Equation 18 provides an alternative approach to solving equations 12 and 13 directly, one that is based upon the use of a numerical simulator. Specifically, it is assumed that a numerical simulator, such as TOUGH2 (Pruess et al., 1999), can be used to find both $c(\mathbf{x},t)$ and $\mathbf{q}(\mathbf{x},t)$ in 18. Thus, equations 12 and 13 decouple and one may find the trajectory solely by solving equation 12. Such an approach can be used to find the trajectories easily from a numerical reservoir simulation in cases where computation time and numerical dispersion are not concerns. A complete specification of the path requires a set of initial conditions, such a source location and the initial angle at which the trajectory leaves the source. Alternatively, one could specify two boundary conditions, such as the initial and final points of the path.

## 3 Applications

In this section we apply the new method for calculating solute trajectories to several examples. Unlike earlier asymptotic approaches for calculating the paths (Vasco et al., 2016), a method based upon equation 12 does not make assumptions regarding the smoothness of macroscopic spatial variations in medium properties. To illustrate this, we examine trajectories for a layer with sharp boundaries, a common occurrence in the subsurface. We also consider the implications of a modified dispersion tensor proposed by Pride et al. (2017) for the solute paths. Finally, we describe a three-dimensional tomographic imaging experiment where solute arrival times are used to estimate the variations in effective permeability in a sandstone core sample.

## 3.1 Solute Transport Within and Around a Layer

In geologic settings the most abrupt changes in material properties are due to interfaces, layering, and fractures. Here we will consider variations in properties that mimic a layer. In this particular subsection we adopt the conventional form of the dispersion tensor, given by equation A5 in Appendix A

$$\mathbf{D} = D_L \mathbf{I} + (D_L - D_T)\,\hat{\mathbf{q}}\hat{\mathbf{q}},$$

where $D_L$ and $D_T$ are the longitudinal and transverse dispersion coefficients. Starting with this representation of the dispersion tensor will facilitate comparisons with previous work (Vasco et al., 2016) and will provide a baseline for our study of the effects of the modified dispersion tensor given in the next subsection (see equation A7 in Appendix A).

Layering is probably the most common source of rapid transitions in a geologic medium. In order to simplify the situation, we consider a single high-permeability zone bounded above and below by half-spaces. As a model of the transitions at the upper and lower boundaries of the zone, consider a medium with vertically varying permeability

$$K(z) = \chi(z) K_o \quad (19)$$

where $K_o$ is a constant background permeability and $\chi(z)$ is a multiplier of the form

$$\chi(z) = 1 - \tfrac{1}{2} \arctan\left[\sigma\,(z - z_i)\right] \quad (20)$$

where $z_i$ specifies the depth of the interface. The parameter $\sigma$ signifies the sharpness of the boundary, larger values correspond to interfaces that more closely resemble a step change in properties. A combination of such steps can be used to describe a compact zone with step-like changes in properties, as plotted in Figure 1. The parameters were chosen such that the permeability within the layer is an order-of-magnitude greater than the background medium. Note that the linear feature might also represent a high-permeability fault zone, and we could consider the panels in Figure 1 to be horizontal slices through the fault.

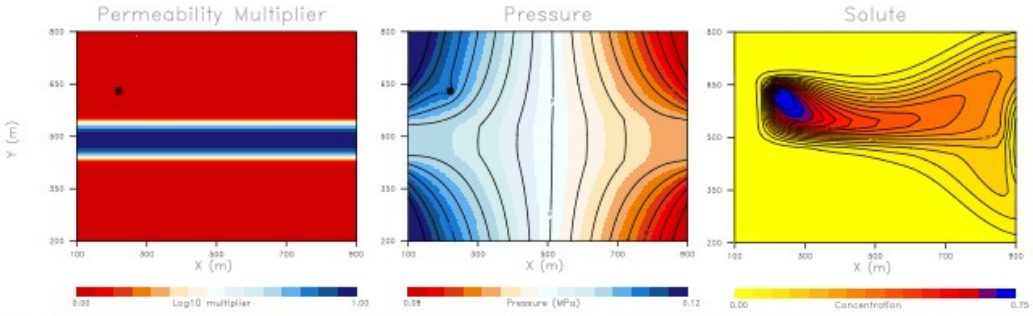


**Figure 1.** (left panel) Cross section through a model consisting of a single layer of higher permeability. The filled square indicates location of the solute injection. (middle panel) Steady state pressure distribution corresponding to injection at a constant flow rate in each grid block at the left end of the model and constant withdrawal from each grid block at the right edge. (right panel) Solute concentration after 125 days of injection.

We will consider tracer injected at a single source point, indicated by the filled square in Figure 1. The left edge of the medium is subject to uniform injection in each grid block, of a cubic meter per second, while the right edge experiences uniform fluid withdrawal of equal magnitude. The injection and production from the grid blocks at the left and right edges results in the spatially varying pressure field shown in Figure 1. The dispersive properties of the medium are a longitudinal dispersitivity ($\alpha_l$ in equation A6 of Appendix A) of 20.0 m, a transverse dispersitivity ($\alpha_t$) of 2.0 m, and negligible molecular diffusion. We calculate the solute concentration after 125 days of injection using the numerical TOUGH2 simulation and plot it in Figure 1, and as the background in Figure 2. The two-dimensional dispersion module T2DM for TOUGH2 has been verified against analytic calculations and compared with different numerical approaches (Oldenburg & Pruess, 1993, 1994, 1995, 1996). We also compared the solute spreading against analytical estimates (Cleary & Ungs, 1978; Javandel et al., 1984), as in Vasco et al. (2016), and found satisfactory agreement. The solute concentration migrates toward the high-permeability layer and advances to the right-hand side under the influence of the flow field. The low permeabilities outside the layer lead to larger pressure drops at the right-hand side of the simulation grid, away from the layer. Thus, the concentrations bifurcate out of the high-permeability zone with the majority moving up and out of the layer near the right edge. However, a notable fraction does travel through the zone, emerging on the opposite side, migrating to a low-pressure area. In Figure 2 we compare the streamlines, representing flow from the injection well to the rightmost edge of the model, and the extended trajectories, representing solute migration from the source to the sinks at the right edge of the model. We calculated 20 trajectories covering an angular range of ±180°. In the left panel we plot the trajectories calculated using the streamline expression 14. The streamlines, determined solely by the flow field, are deflected into the high-permeability layer. In the panel on the right in Figure 2 we display the extended trajectories. The extended trajectories indicate solute movement to both the upper and lower half-spaces, in keeping with the concentrations from the numerical simulation.

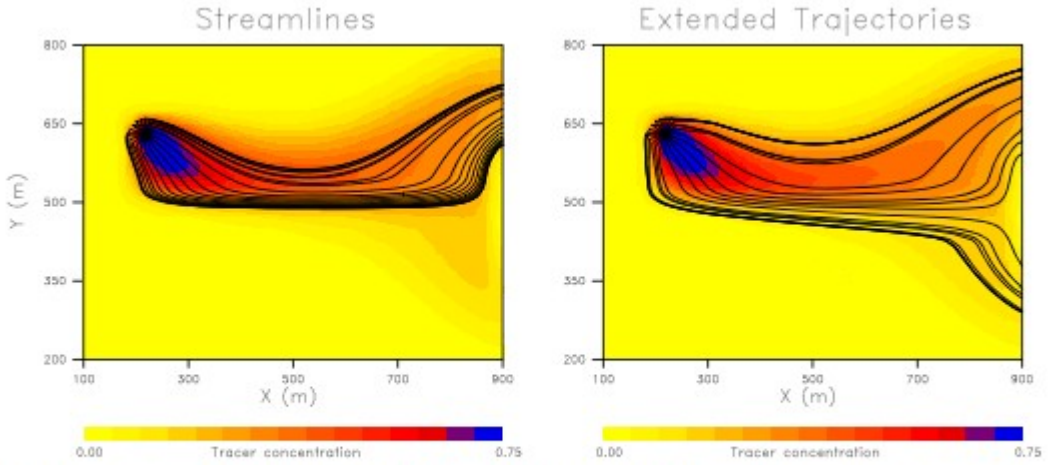


**Figure 2.** Trajectory calculations based upon the permeability model shown in Figure 1. A comparison between (left panel) trajectories computed using a streamline approach, equation (14) and (right panel) the extended trajectories based upon a full reservoir simulation and equation (15).

### 3.2 The Influence of an Asymmetric Dispersion Tensor on Solute Transport

As was pointed out by Koch and Brady (1987), Auriault et al. (2010), and Pride et al. (2017), the dispersion tensor is asymmetric and the conventional representation (as in equation A5 in Appendix A) is incomplete. We provide a more in-depth discussion of these considerations in Appendix A. In this subsection we consider the implications of adopting the modified form A7,

$$\mathbf{D} = D_L \mathbf{I} + (D_L - D_T)\,\hat{\mathbf{q}}\hat{\mathbf{q}} + a\left[\nabla\mathbf{q} - (\nabla\mathbf{q})^T\right]$$

proposed by Pride et al. (2017) to account for the asymmetry of the dispersion tensor. The parameter *a* has units of length squared and depends upon the Peclet number of the flow field (Pride et al., 2017). The single-layer model shown in Figure 1, and described above, is adopted as a reservoir model as this will facilitate comparisons with our previous work involving the symmetric dispersion tensor. Because the heterogeneity is two-dimensional, there will be two nonzero off-diagonal terms, which are denoted as $D_{12}$ and $D_{21}$, where the index 1 signifies the *x* (horizontal) coordinate and the index 2 signifies the *z* (vertical) coordinate. Using the pressure distribution from the TOUGH2 reservoir simulation, we calculated the symmetric component of the off-diagonal term, given by

$$\overline{D_{12}} = \frac{(D_{12}+D_{21})}{2}. \quad (21)$$

The symmetric component of the off diagonal term, $\overline{D_{12}}$, is plotted in Figure 3. The asymmetric contribution to the dispersion tensor, given by the last term on the right-hand side of the representation of **D** given above, is plotted in the right panel of Figure 3. The asymmetric component is a significant contribution to the overall dispersion tensor and is concentrated at the boundaries of the layer, where the heterogeneity is large. At the layer edges the flow field is changing rapidly and the spatial derivatives of the

components of **q** are largest. The trajectories, computed using equation 12, with **D** given above, are shown in Figure 4 for two different values of *a*. Using the formula presented in Pride et al. (2017), values of $a$ = 100 and 1,000 $m^2$ correspond to Peclet numbers of 22.4 and 0.01, respectively. Comparing the trajectories in Figure 4 to those in Figure 2, it appears that the additional term in the dispersion tensor causes the solute paths to diverge at the top of the layer and to converge at the bottom of the layer, leading to a general concentration of solute paths near the base of the layer. The effect is not strong, however, and only occurs for relatively low Peclet numbers.

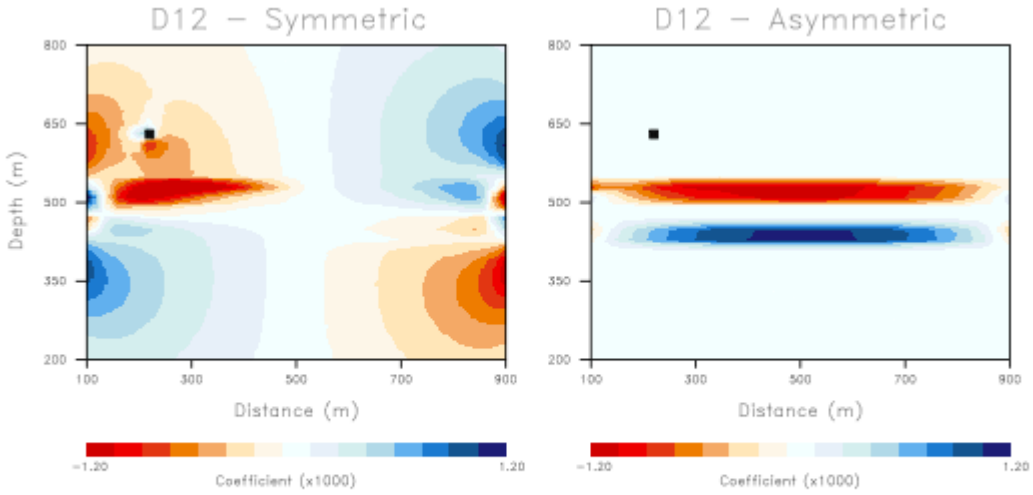


**Figure 3.** (left panel) Symmetric component of the off-diagonal coefficient $D_{12}$ of the dispersion tensor, given by $\overline{D_{12}} = (D_{12} + D_{21})/2$. (right panel) Asymmetric contribution to the off-diagonal component $D_{12}$, given by $a\left[\nabla \mathbf{q} - (\nabla \mathbf{q})^T\right]$.

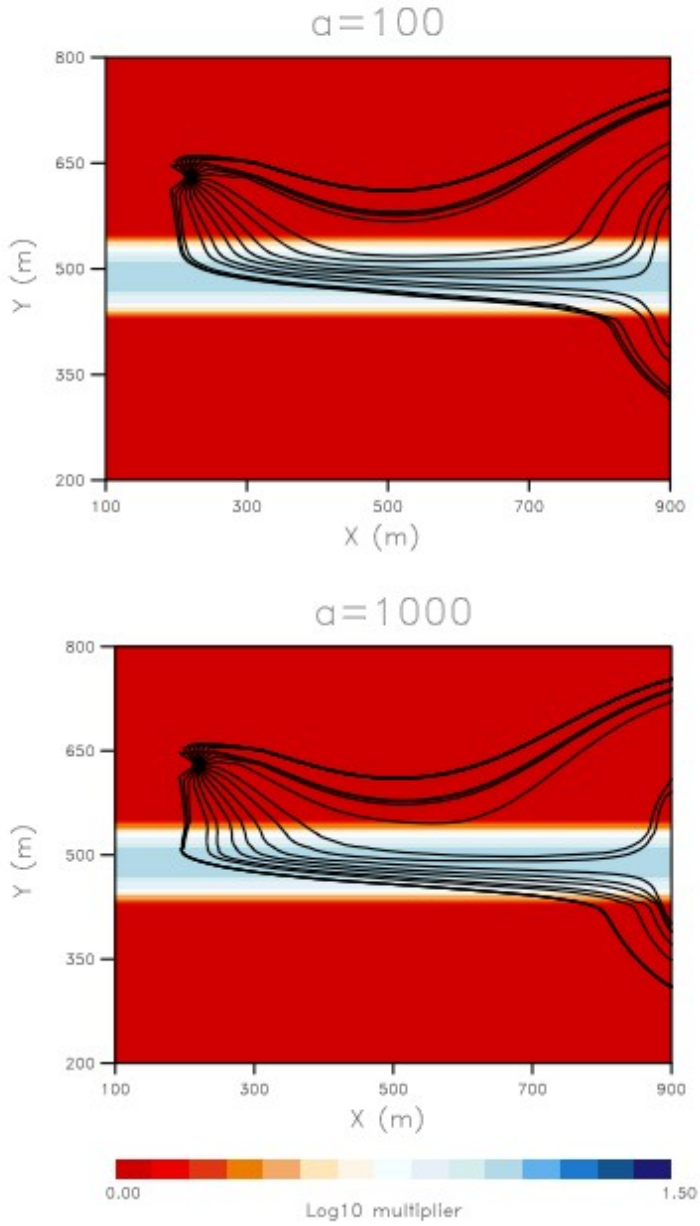


**Figure 4.** Trajectories calculated using the extended trajectory approach for the layer model in Figure 1 but using the modified expression (A7) for the dispersion tensor **D**. Twenty trajectories are calculated, covering an angular range of ±140°. The two panels correspond to $a$ = 100 and 1,000 $m^2$, respectively.

### 3.3 Positron Emission Tomographic Monitoring of Solute Movement

One useful application of the extended trajectories is the estimation of variations in the hydraulic conductivity of a porous medium (Datta-Gupta et al., 2002; Vasco & Datta-Gupta, 1999, 2016; Vasco & Finsterle, 2004; Vasco et al., 2016). We make use of the expression for the trajectory, equation 18, to derive a semianalytical expression for the solute travel time. Specifically, we can combine equations 1b and 18, to arrive at

$$\frac{\mathrm{d}\mathbf{x}}{\mathrm{d}t} = \mathbf{v} = -\frac{1}{\varphi}\left(\frac{k}{\mu}\nabla p + \nabla \ln c \cdot \mathbf{D}\right). \quad (22)$$

Integrating equation 22 along the trajectory x($t$) produces an explicit expression for the travel time of the solute along the path from the source to an observation point

$$T = -\int_{\mathbf{x}} \frac{\mathrm{d}r}{v}, \quad (23)$$

where

$$v = \frac{1}{\varphi}\left|\frac{k}{\mu}\nabla p + \nabla \ln c \cdot \mathbf{D}\right|, \quad (24)$$

and $r$ is the distance along the trajectory. Equation 23 provides a relationship between the travel time of the solute and the velocity along the trajectory. As we shall see, it can be used to calculate the spatial variations in $\varphi/k$ within a porous medium.

We illustrate the imaging technique using a series of three-dimensional micropositron emission tomography (micro-PET) images of radiotracer concentration. Images were obtained by injecting a pulse of radiotracer at 3 mL/min into a 2-in. diameter Berea sandstone core which was initially saturated with water. The outer boundary of the core was sealed, loaded into a coreholder, and connected to a coreflooding system as described in detail in Zahasky and Benson (2018). Once the PET scan was started, a 4-mL pulse of water containing the radiotracer Fludeoxyglucose (FDG) was injected into the left face, while the right face of the core was kept at a constant pressure of 17 bar. The confining pressure was kept constant at 38 bar. Following the pulse of injected radiotracer, water was injected at the same rate to displace the tracer through the core. During the injection, the core was imaged continuously using a Siemens preclinical Inveon DPET scanner at the Stanford Center for Innovation in In-Vivo Imaging. The detected gamma rays resulting from positron emission were used to reconstruct the radioactivity (concentration) of each volume element (voxel), as a function of time. The time-varying radioactivity was reconstructed into 40-s time frames in order to estimate the change in concentration over time (Figure 5). The PET scan was reconstructed with 3-D Ordered Subset Expectation Maximization using Maximum A Priori (OSEM-OP MAP; Hudson & Larkin, 1994). The scan was reconstructed with voxels 0.77 mm × 0.77 mm × 0.79 mm ($x$, $y$, $z$); however, the images were coarsened to 2.33 mm × 2.33 mm × 2.39 mm by taking the average of nine adjacent voxels. The images were coarsened to this resolution to reduce data noise (Zahasky & Benson, 2018). It is evident that variations in radiotracer advection rates reflect heterogeneities in the core and that the radioactivity arrives in some regions of the core much earlier than in other areas, even though the distances from the injection core face are similar. This suggests that one can use these changes to quantify spatial variations in hydraulic conductivity within the core.

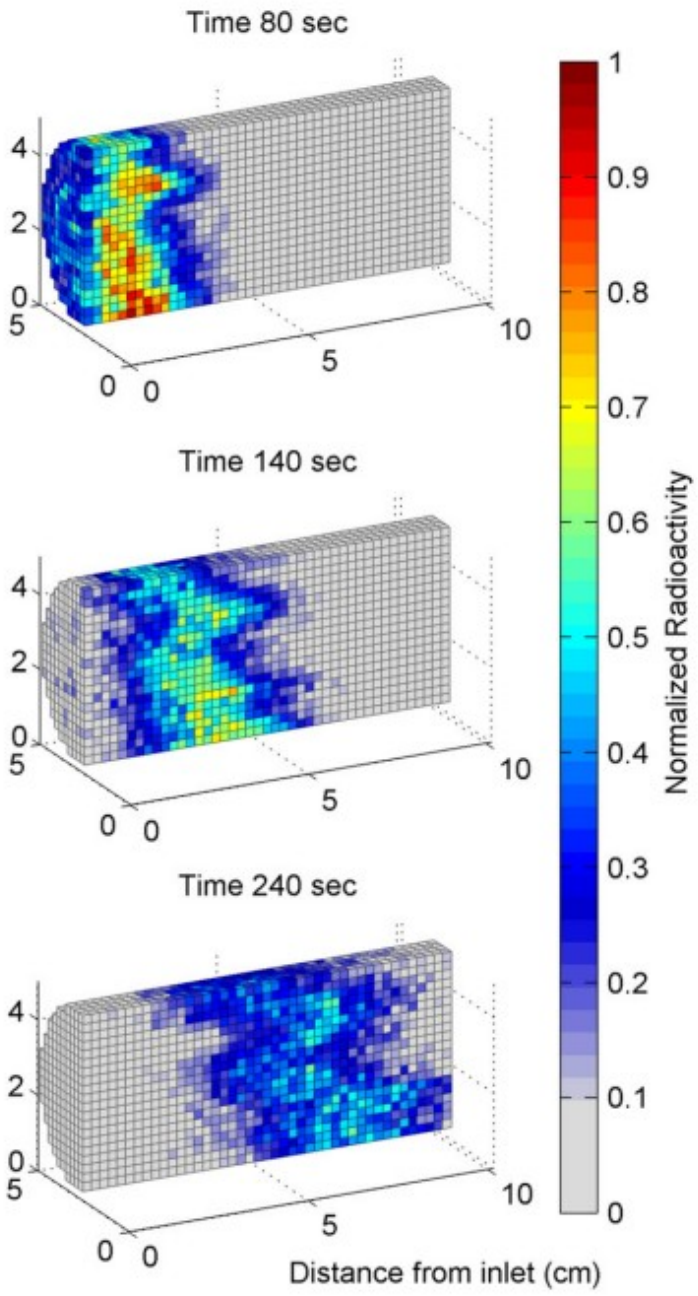


**Figure 5.** Three snapshots of normalized radioactivity variations due to the injection of the radiotracer Fludeoxyglucose into a Berea sandstone core. The color scale in each panel signifies the normalized values over a slice through the center of the sandstone core at three different times.

While it is possible to use the magnitude of the changes in radioactivity to infer the flow properties of the core, the relationship between the magnitude of the computed radioactivity and the magnitude of the concentration change is complicated by factors such as the sample location in the scanner field of view and variations in sample mineral composition, which lead to local variations in photon attenuation. It is more straightforward to use the onset time, the clock time at which an observable starts to change from its background value (Vasco et al., 2014, 2015), as a measure of the arrival

time of the tracer. For this experiment, we define the onset time as that instant when the concentration change attains a peak value in a particular volume element (voxel). Other measures of onset time are possible, including the first temporal moment of the concentration (Harvey & Gorelick, 1995), the time at which the steepest slope is observed, and the time at which the normalized concentration exceeds some threshold, such as 5% of the peak. In order to obtain voxel-scale precision, we fit a quadratic equation to the five points defined by the peak and the four adjacent points of radiotracer concentration for every voxel in the sample. The arrival or onset time is defined by the peak of the quadratic function and the estimated times for the core are shown in Figure 6. The onset or travel times in Figure 6 comprise our basic data set, and we take them as the arrival times of the solute and interpret them using equation 23.

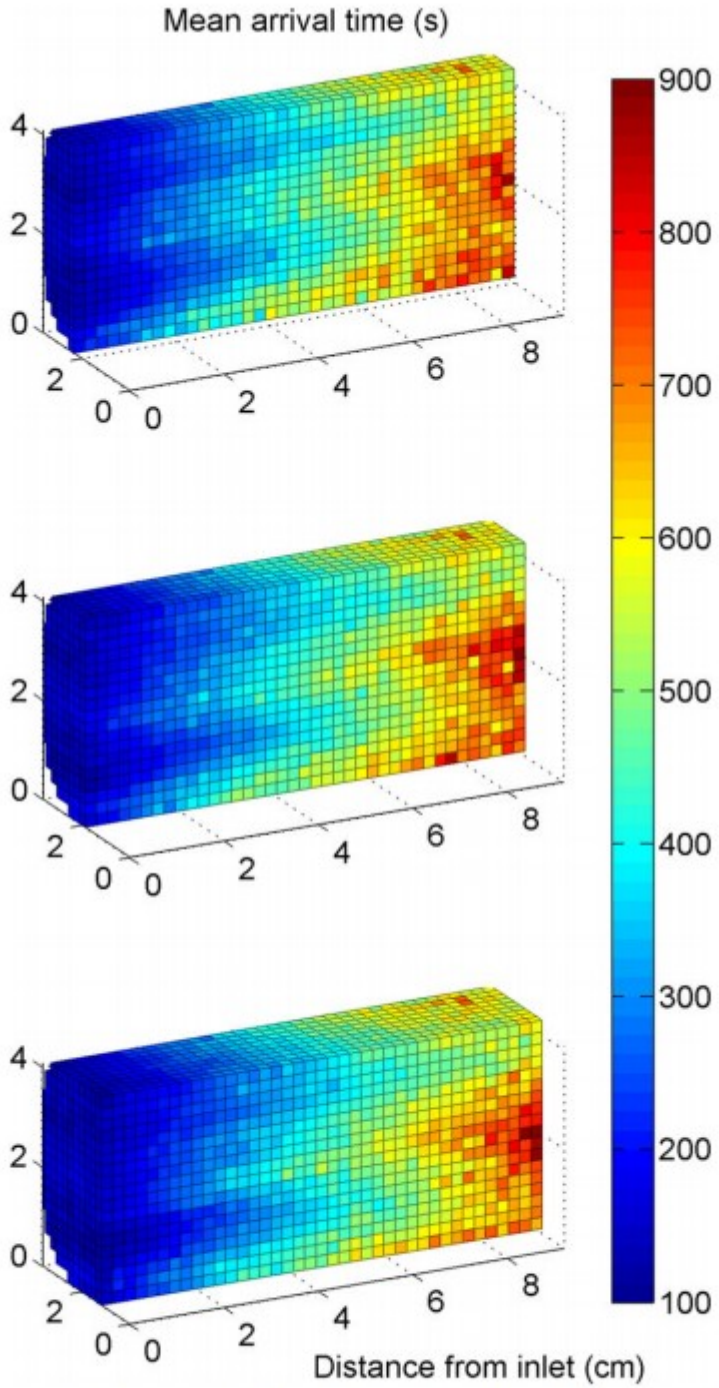


**Figure 6.** Onset time corresponding to changes in the radioactivity in each voxel from their background values for three different vertical slices through the sample core. The onset time is defined as the moment at which the normalized radioactivity reaches the peak value attained in the voxel.

In order to formulate the inverse problem, we discretize the core into the same geometry as the PET images, subdividing the volume into a three-dimension grid of 20 ($x$) by 39 ($y$) by 20 ($z$) grid of nearly cubic cells. We can

then rewrite the integral 23 as a discrete sum over the trajectory segments in each of the grid blocks that the ray traverses

$$T = -\sum_{i \in N} \frac{1}{v_i} L_i = -\sum_{i \in N} s_i L_i \quad (25)$$

where $v_i$ is the average velocity in the $i$th grid block, $L_i$ is the length of the trajectory in cell $i$, and $s_i$ is the inverse of the velocity ($1/v_i$), known as the slowness. The trajectories are derived from a numerical simulation based upon the initial model of the porous medium. That is, the flow properties, the pressure field, and the concentration fields as a function of time, are used along with equation 22 to calculate the trajectory $\mathbf{x}(t)$. If the initial flow properties are taken to be constant throughout the core, then the initial trajectories will be straight lines parallel to the axis of the core, given a uniform flow field from the inlet to the outlet. Formulating the inverse problem in terms of slowness, $s_i$, produces sensitivity coefficients that are constant for each grid block. In contrast, formulating the inverse problem in terms of velocity introduces a $1/v_i^2$ term in the sensitivities, potentially leading to instabilities in any inversion as $v_i$ tends toward large or small values.

One calculates an expected travel time based upon an initial simulation model of velocity or slowness and then writes an expression for travel time deviations in terms of slowness perturbations. That is, an expression for the model parameter sensitivity follows if we consider a small perturbation in the slowness of the $i$th grid block, $\delta s_i$, with respect to an initial or background slowness value $s_i^o$ , then

$$\mathrm{T} = \mathrm{T}^o + \delta T = -\sum_{i \in N} \left( s_i^o + \delta s_i \right) L_i$$

The quantity $\delta T$ is the difference between the travel time and the travel time in the initial model, $T^o$. Subtracting $T^o$ from both sides and using the fact that the initial model generates this travel time:

$$T^o = -\sum_{i \in N} s_i^o L_i,$$

leads to

$$\delta T = -\sum_{i \in N} L_i \delta s_i. \quad (26)$$

The sensitivity for the $i$th model parameter is the coefficient associated with $\delta s_i$, that is $L_i$, the length of the trajectory in the $i$th grid block.

Because the trajectory $\mathbf{x}(t)$, and hence the set of grid blocks intersected by the path, depends upon the slowness distribution, the relationship between the solute arrival time and the slowness is still nonlinear. However, it can be linearized if the slowness changes are not large in relation to the background value $\bar{s}_i$ . If the changes are large, we can adopt an iterative approach to solve the system of equations, starting with a uniform distribution of

properties and run the reservoir simulator TOUGH2 (Oldenburg & Pruess, 1995) to calculate $p(\mathbf{x},t)$ and $c(\mathbf{x},t)$ and the trajectories $\mathbf{x}(t)$ from each observation point. An updated conductivity is calculated at each iteration and the reservoir simulator is rerun with the new model.

Given a large set of travel times, we may solve for the velocity, or the slowness, in each voxel. Each travel time provides a constraint, such as equation 26, on the slownesses of the subset of grid blocks that the path traverses. For each observation point there is a trajectory from that location to a source point located on the inlet. Given a collection of arrival times to each sample point, we may write the resulting linear system of equations in vector matrix form

$$\delta \mathbf{T} = \mathbf{M}\delta \mathbf{s}, \quad (27)$$

where $\mathbf{M}$ is the matrix containing the coefficients in equation 26, the trajectory lengths in each grid block, and $\delta\mathbf{s}$ is the update to the current slowness model vector. We may use the method of penalized least squares (Menke, 1989) to solve the system for the vector of unknowns $\delta\mathbf{s}$. We applied the linearized inversion approach to the micro-PET data obtained during the injection experiment. Neglecting the voxels that are outside of the sample there are a total of 12,251 arrival times within the core, providing a large system of equations. The first step of the inversion algorithm produced a three-dimensional distribution of solute slownesses $s(\mathbf{x})$. From the slowness we may extract the velocity and use equation 24 to solve for the permeability in terms of the velocity and quantities estimated from the numerical simulator

$$k = -\frac{\mu}{|\nabla P|}\left|\varphi v - \nabla \ln c \cdot \mathbf{D}\right| \cdot \quad (28)$$

When the dispersion is negligible or the concentration is uniform in the medium, the second term on the right vanishes and the permeability estimate is identical to that provided by Darcy's law (de Marsily, 1986). In that case this trajectory is identical to a streamline. Equation 28 provides an estimate of the effective permeability because any variations in porosity will also map into $k$. Other methods, such as X-ray imaging or ultrasonic methods, may be used to estimate the porosity variations and incorporate them into expression 28. For the Berea sandstone core used in this study, the porosity variations were fairly uniform, with values of around 20% based upon 3-D porosity maps obtained with a clinical CT scanner (Akin & Kovscek, 2003). The estimated permeability variations, obtained from equation 28, are plotted in Figure 7. Note the generally higher permeability near the base of the core and the subhorizontal elongated anomalies suggestive of layering. Selected trajectories associated with the heterogeneous model (Figure 7) are plotted in Figure 8. The trajectories are largely along the axis of the core, but the bending of the paths due to the permeability variations is evident both in the top and side views.

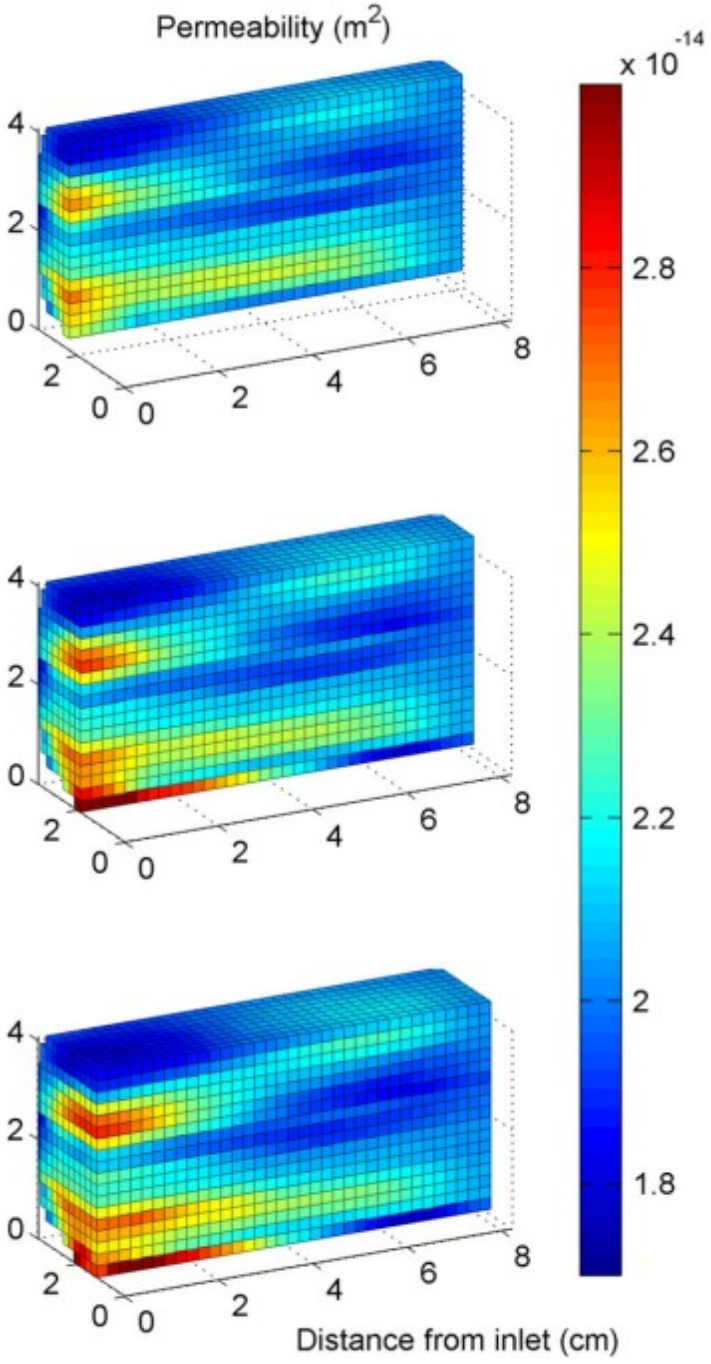


**Figure 7.** Three slices through the core, showing the intrinsic permeability estimated from an inversion of the micro-PET arrival times.

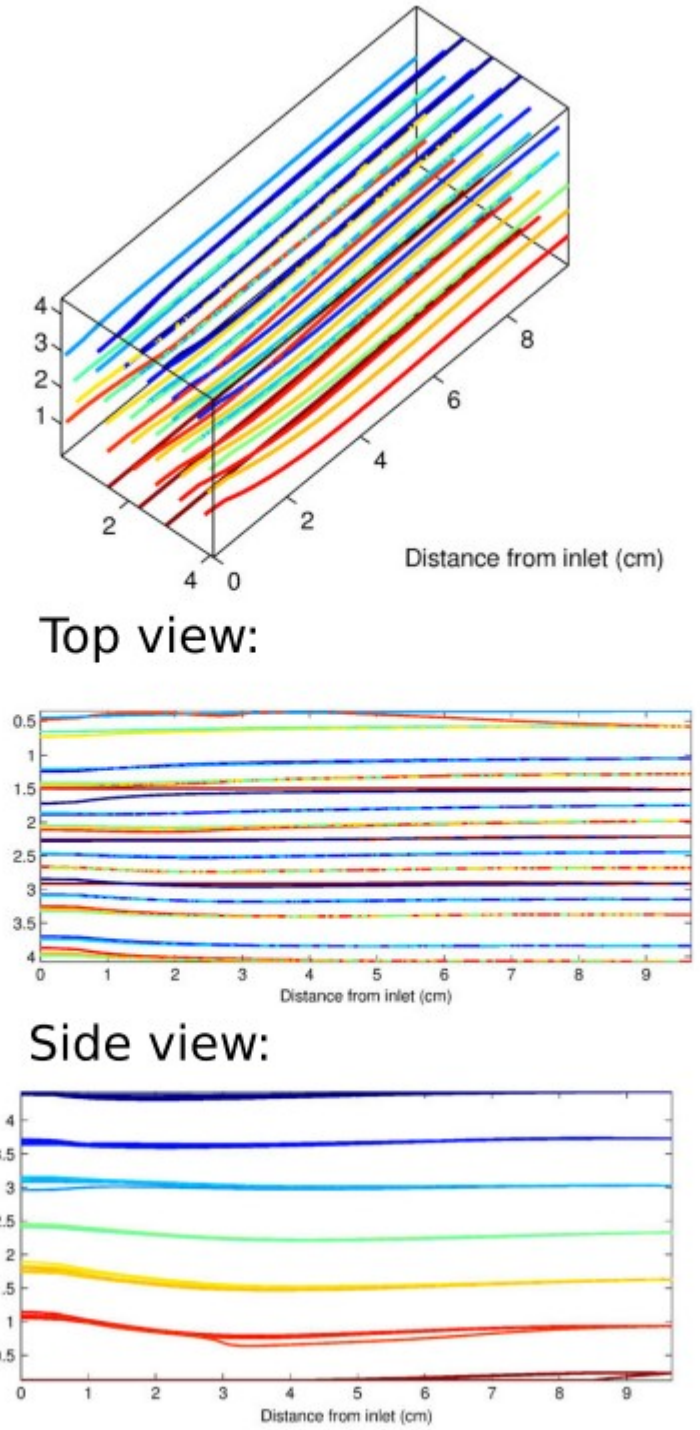


**Figure 8.** Three different views of selected trajectories associated with flow in the updated core model shown in Figure 7.

## 4 Conclusions

We have described a trajectory-based approach for modeling solute transport in a flow field. The trajectories may be used for visualization or as the basis for a tomographic-like imaging algorithm. No assumptions about

the smoothness of the medium are made in the derivation and the trajectories are valid for spatial variations that contain sharp boundaries, an improvement over existing asymptotic techniques (Vasco et al., 2016). Unlike streamline methods, the trajectories are influenced by molecular diffusion and the dispersivities of the porous medium. A comparison between streamlines and the extended trajectories in a medium containing a layer illustrates the influence of transverse dispersitivity on the paths of the solute. By incorporating the output of a numerical simulator, one may calculate the trajectories using a straightforward integration. The technique is applicable to other processes, such as the study of transient pressure propagation (Vasco, 2018).

Recent work (Auriault et al., 2010; Pride et al., 2017) supported the conclusion of Koch and Brady (1987) that the dispersion tensor **D** is asymmetric, and we explored the implications of the form proposed by Pride et al. (2017). A model containing a high-permeability layer indicated that the asymmetry is only significant locally, where the heterogeneity is significant. These results are in agreement with the observation of Carbonell and Whitaker (1983) and Amaral Souto and Moyne (1997) that the antisymmetric component of the dispersion tensor is annihilated in a homogeneous medium, as discussed in Appendix A. For the case under consideration, the significant spatial variations were at the top and bottom edges of the layer. For the heterogeneous model containing a layer the modifications of the dispersion tensor had the effect of concentrating the flow of the solute in the high-permeability layer.

The semianalytic expression for solute travel time provided by this approach leads to an imaging algorithm for estimating hydraulic conductivity in heterogeneous geologic porous media. This imaging technique is illustrated using solute arrival times measured experimentally with micro-PET monitoring of radioctivity changes due to the injection of a radiotracer in a heterogeneous sandstone core. For tests involving a single injection site, only one numerical simulation is needed in order to compute sensitivities for all observations. The method is well suited for geophysical time-lapse monitoring of tracer tests where a number of snapshots of the concentration distribution are imaged. Such monitoring has been shown to be feasible (Becker & Tsoflias, 2010; Day-Lewis et al., 2003; Tsoflias & Becker, 2008) and should become more common as automated data collection systems are developed (Daley et al., 2011). As demonstrated in the PET images, given a sufficient number of snapshots, one can construct the distribution of fluid arrival times and from this infer the hydraulic conductivity. In this regard, the concept of onset time, the time at which a geophysical attribute begins to change from its background value, is useful in reducing the series of geophysical images to a single map of values (Vasco et al., 2014, 2015, 2016). From the map of onset times it is possible to infer hydraulic conductivity in a stable fashion as shown in Vasco et al. (2016) and in the application above.

Acknowledgments

Theoretical work, formulation, synthetic testing, and data inversion performed at Lawrence Berkeley National Laboratory was supported by the U.S. Department of Energy under contract DE-AC02-05-CH11231, Office of Basic Energy Sciences. Experimental work was funded by the Global Climate Energy Project, the Stanford Center for Carbon Storage, and the Department of Energy Resources Engineering. The Inveon DPET (micro-PET) scanner was funded by NIH grant 1S10OD018130-01. The micro-PET normalized radioactivity data for the core plug experiment are available from the public data sharing site Zenodo by accessing the file using the digital identifier doi 10.5281/zenodo.1299325 and in the Stanford Digital Repository accessible through the link https://purl.stanford.edu/wj853cz6083.

## Appendix A: The Nature of the Dispersion Tensor

The physical characteristics of solute transport have been studied extensively, from the early experiments of Slichter (1905) and mathematical descriptions of the flow in capillary tubes by Taylor (1953) and Aris (1956), to the present day (Fel & Bear, 2010; Liu & Kitanidis, 2013; Pride et al., 2017). The study by Scheidegger (1954), in which the term dispersivity was introduced, appears to be the first statistical treatment of the hydrodynamics of solute transport. Soon after, de Jong (1958) completed a statistical analysis that accounted for the variations of the pressure gradient in channels due to differences in their orientations with respect to the direction of the macroscopic flow field. This led to the conclusion that dispersion in the direction parallel to the flow field (longitudinal dispersion) is greater than dispersion transverse to the direction of the flow field (transverse dispersion), even if the flow properties of the medium are isotropic. Saffman (1959) extended the statistical approach by explicitly including molecular diffusion in the model, in addition to mechanical dispersion. Bear (1961) analysis, based upon the finding of de Jong (1958), that the solute distribution from a point injection in a uniform flow field approximates a bivariate normal distribution, emphasizes that the dispersion is described by a second-rank tensor. By extending Bear (1961) analysis to uniform flow within an isotropic medium, de Jong and Bossen (1961) deduced the form

$$\mathrm{D}_{ij} = a_{klij}\frac{V_k V_l}{V}, \quad \text{(A1)}$$

where $a_{klij}$ is a fourth-rank tensor of dispersion coefficients, $V_k$ are the flow velocity vector components, and $V$ is the flow velocity magnitude. They also derive a governing equation for dispersive solute transport, written in terms of $D_{ij}$. Note that **D** scales as the flow velocity magnitude $V$, as was observed experimentally (Scheidegger, 1961). A similar expression was derived by Nikolaevskii (1959) who drew from the statistical studies of turbulence, using a theorem stating that a point tensor of dispersion must have even rank when the medium is isotropic. Nikolaevskii adopts the representation A1 as the simplest form consistent with this requirement. Other studies, based

upon averaging techniques (Amaral Souto & Moyne, 1997; Carbonell & Whitaker, 1983; Koch & Brady, 1985) and asymptotic approaches, such as the method of multiple scales (Koch & Brady, 1987) and homogenization (Auriault et al., 2010; Hornung, 1997; Mei, 1992; Rubinstein & Mauri, 1986) have shown that the dispersion tensor is of the general form

$$\mathbf{D} = d_m (\mathbf{I} + \tau) + \mathbf{A}_{\text{dis}} \quad \text{(A2)}$$

where $d_m$ is the molecular diffusion, $\tau$ is the tortuosity tensor (Amaral Souto & Moyne, 1997; Carbonell & Whitaker, 1983), and $\mathbf{A}_{\text{dis}}$ is the hydrodynamic dispersion tensor that depends in a nonlinear fashion upon the flow field **q**. The exact nature of the dependence of $\mathbf{A}_{\text{dis}}$ upon $q$, the magnitude of **q**, or on the Peclet number $Pe = ql/d_m$, where $l$ is the diameter of the grains in a porous medium, has not been definitively established. An asymptotic analysis, in the limit of a low volume fraction of fixed spheres, produced estimates that contained terms of order $Pe$, $Pe^2$, and $Pe \ln Pe$, depending upon the nature of the flow (Koch & Brady, 1985). Fits to laboratory data identified five flow regimes in which longitudinal dispersion took on various forms (de Marsily, 1986, p. 237; Delgado, 2007).

Scheidegger (1961) provided an early discussion of the symmetry properties of the dispersion matrix. He relied upon an admittedly naive application of Onsager's principle of microscopic reversibility (Onsager, 1931a, 1931b) to justify the symmetry of **D**. Koch and Brady (1987) present a rigorous application of Onsager's relations to show that an asymmetric component of the tensor **D** may exist in a medium lacking three orthogonal planes of reflective symmetry. It was pointed out by Carbonell and Whitaker (1983) and Amaral Souto and Moyne (1997) that if **D** does not vary in space, then equation 1a becomes

$$\mathbf{D}\nabla\nabla c - \nabla \cdot (\mathbf{q}c) = \varphi \frac{\partial c}{\partial t}. \quad \text{(A3)}$$

Due to the symmetry of the operator $\nabla\nabla c$, any antisymmetric component of the dispersion tensor will be annihilated and will not influence the evolution of the solute concentration. Note that this argument only applies to a homogeneous medium with a flow field that does not vary in space. In the presence of inhomogeneities the dispersion tensor **D** may well be asymmetric. The lack of sensitivity in the case of a homogeneous medium may explain why it has often been assumed that the dispersion tensor is symmetric. The asymmetry of the dispersion tensor pointed out by Koch and Brady (1987) has been confirmed by Auriault et al. (2010) using a homogenization technique for low Peclet number flows. They also verified a symmetry associated with a reversal of the flow field **q**,

$$D_{ij}(\mathbf{q}) = D_{ji}(-\mathbf{q}). \quad \text{(A4)}$$

The asymmetry of the dispersion tensor was demonstrated by Pride et al. (2017) for general flow conditions. The symmetry under flow reversal,

equation A4, was derived by Pride et al. (2017), and verified by Flekkoy et al. (2017), without imposing the conditions of Auriault et al. 2010.

A general form of the dispersion tensor that incorporates many of the ideas reflected in equations A1 and A2 is the widely used representation

$$\mathbf{D} = D_L \mathbf{I} + (D_L - D_T)\,\hat{\mathbf{q}}\hat{\mathbf{q}} \quad \text{(A5)}$$

where $\hat{\mathbf{q}}$ is a unit vector in the direction of **q**, $D_L$ and $D_T$ are the longitudinal and transverse dispersion coefficients, given by

$$D_L = \frac{d_m}{F} + \alpha_l q$$

$$D_T = \frac{d_m}{F} + \alpha_t q \quad \text{(A6)}$$

where $F$ is the formation factor (de Marsily, 1986, p. 34), and $\alpha_l$ and $\alpha_t$ are the longitudinal and transverse dispersivities (Oldenburg & Pruess, 1995). The formation factor is given by $F = 1/\varphi\tau$ in Oldenburg and Pruess (1995) where $\tau$ is the tortuosity, the ratio of diffusion in the porous medium to diffusion in the fluid (de Marsily, 1986, p. 233).

Note that **D** given by expression A5 is symmetric, in contrast to the findings of Koch and Brady (1987), Auriault et al. (2010), and Pride et al. (2017). Pride et al. (2017) suggest a modification of A5,

$$\mathbf{D} = D_L \mathbf{I} + (D_L - D_T)\,\hat{\mathbf{q}}\hat{\mathbf{q}} + a\left[\nabla\mathbf{q} - (\nabla\mathbf{q})^T\right] \quad \text{(A7)}$$

that satisfies equation A4 and displays the appropriate asymmetry. The parameter $a$ has units of length squared and numerical Lattice-Boltzmann computations in Pride et al. (2017) indicate that it is a function of the Peclet number. The form A7 reflects that fact that if flow differs in magnitude in adjacent regions, there will be off-diagonal components in the dispersion tensor. Simulations based upon Lattice-Boltzmann computations are consistent with a dispersion tensor of the form A7 (Pride et al., 2017).

References

Akin, S., & Kovscek, A. R. (2003). Computed tomography in petroleum engineering research. In F. Mees, R. Swennen, M. Van Geet, & P. Jacobs (Eds.), *Applications of X-ray computed tomography in the geosciences* (Vol. 215, pp. 243). London: Geological Society of London, Special Publications.

Amaral Souto, H. P., & Moyne, C. (1997). Dispersion in two-dimensional periodic porous media. Part II. Dispersion tensor. *Physics of Fluids*, 9, 2253–2263.

Aris, R. (1956). On the dispersion of solute in a fluid flowing through a tube. *Proceedings of the Royal Society A*, 235, 67– 77.

Auriault, J.-L., Moyne, C., & Amaral Souto, H. P. (2010). On the asymmetry of the dispersion tensor in porous media. *Transport in Porous Media*, 85, 771–783. https://doi.org/10.1007/s11242-010-9591-y

Bear, J. (1961). On the tensor form of dispersion in porous media. *Journal of Geophysical Research*, 66, 1185– 1197.

Bear, J., & Verruijt, A. (1987). *Modeling groundwater flow and pollution*. Norwell, MA: D. Reidel.

Becker, M. W., & Tsoflias, G. P. (2010). Comparing flux-averaged and resident concentration in a fractured bedrock using ground penetrating radar. *Water Resources Research*, 46, W09518. https://doi.org/10.1029/2009/WR008260

Bittner, E. R., Kouri, D., Derrickson, S., & Maddox, J. (2010). Variational quantum hydrodynamics. In X. Oriols & J. Mompart (Eds.), *Applied Bohmian dynamics: From nanoscale systems to cosmology* (pp. 303– 364). Singapore: Pan Stanford Publishing.

Bratvedt, F., Gimse, T., & Tegnander, C. (1996). Streamline computations for porous media flow including gravity. *Transport in Porous Media*, 25, 63– 78.

Carbonell, H. B. G., & Whitaker, S. (1983). Dispersion in pulsed systems—II. Theoretical developments for passive dispersion in porous media. *Chemical Engineering Science*, 38, 1795– 1802.

Cash, J. R., & Carp, A. H. (1990). A variable order Runge-Kutta method for initial value problems with rapidly varying right-hand sides. *ACM Transactions on Mathematical Software*, 16, 201– 222.

Chapman, S. J., Lawry, J. M. H., & Ockendon, J. R. (1999). Ray theory for high-Peclet-number convection diffusion. *SIAM Journal of Applied Mathematics*, 60, 121– 135.

Cirpka, O. A., de Barros, F. P. J., Chiogna, G., Rolle, M., & Nowak, W. (2011). Stochastic flux-related analysis of transverse mixing in two-dimensional heterogeneous porous media. *Water Resources Research*, 47, W06515. https://doi.org/10.1029/2010WR010279

Cleary, R. W., & Ungs, M. J. (1978). Groundwater pollution and hydrology, mathematical models and computer programs (Report 78-WR-15). Princeton, NJ: Water resource program, princeton university.

Coscia, I., Linde, N., Greenhalgh, S., Vogt, T., & Green, A. (2012). Estimating traveltimes and groundwater flow patterns using 3-D time-lapse crosshole ERT imaging of electrical resistivity fluctuations induced by infiltrating river water. *Geophysics*, 77, E239– E250.

Crane, M. J., & Blunt, M. J. (1999). Streamline-based simulation of solute transport. *Water Resources Research*, 35, 3061– 3078.

Dagan, G. (1982). Stochastic modeling of groundwater flow by unconditional and conditional probabilities: 2. The solute transport. *Water Resources Research*, 18, 835– 848.

Dagan, G. (1987). Theory of solute transport by groundwater. *Annual Reviews of Fluid Mechanics*, 19, 183– 215.

Dagan, G., & Cvetkovic, V. (1996). Reactive transport and immiscible flow in geological media: I. General theory. *Proceedings of the Royal Society of London Series A*, 452, 285– 301.

Daley, T. M., Ajo-Franklin, J. B., & Doughty, C. (2011). Constraining the reservoir model of an injected $CO_2$ plume with crosswell CASSM at the Frio-II brine pilot. *International Journal of Greenhouse Gas Control*, 5, 1022– 1030.

Datta-Gupta, A., & King, M. J. (1995). A semianalytic approach to tracer flow modeling in heterogeneous permeable media. *Advances in Water Resources*, 18, 9– 24.

Datta-Gupta, A., & King, M. J. (2007). *Streamline simulation: Theory and practice*. Society of Petroleum Engineers, Richardson.

Datta-Gupta, A., Lake, L. W., Pope, G. A., Sephernoori, K., & King, M. J. (1991). High-resolution monotonic schemes for reservoir fluid flow simulation. *In Situ*, 15( 3), 289– 317.

Datta-Gupta, A., Yoon, S., Vasco, D. W., & Pope, G. A. (2002). Inverse modeling of partitioning interwell tracer tests: A streamline approach. *Water Resources Research*, 38( 6), 1079– 1029.

Day-Lewis, F. D., Lane, Jr. J. W., Harris, J. M., & Gorelick, S. M. (2003). Time-lapse imaging of saline-tracer transport in fractured rock using difference-attenuation radar tomography. *Water Resources Research*, 39, 1290. https://doi.org/10.1029/2002WR001722

de Jong, G. (1958). Longitudinal and transverse diffusion in granular deposits. *Transactions of the American Geophysical Union*, 39, 67– 74.

de Jong, G., & Bossen, M. L. (1961). Discussion of paper by Jacob Bear, “On the tensor form of dispersion in porous media”. *Journal of Geophysical Research*, 66, 3623– 3624. https://doi.org/10.1029/JZ066i010p03623

de Marsily, G. (1986). *Quantitative hydrogeology*. San Diego, CA: Academic Press.

Delgado, J. M. P. Q. (2007). Longitudinal and transverse dispersion in porous media. *Transactions IChemE*, 85, 1245– 1252.

Doetsch, J., Linde, N., Vogt, T., Binley, A., & Green, A. G. (2012). Imaging and quantifying salt-tracer transport in a riparian groundwater system by means of 3D ERT monitoring. *Geophysics*, 77, B207– B218.

Fay, C. H., & Pratts, M. (1951). The application of numerical methods to cycling and flooding problems. In *Proceedings of the 3rd world petroleum congress* (pp. 101– 112). New York: John Wiley.

Fel, L., & Bear, J. (2010). Dispersion and dispersivity tensors in saturated porous media with uniaxial symmetry. *Transport in Porous Media*, 85, 259–268.

Flekkoy, E. G., Pride, S. R., & Toussaint, R. (2017). Onsager symmetry from mesoscopic time reversibility and the hydrodynamic dispersion tensor for coarse-grained systems. *Physical Review E*, 95, 1– 8.

Fogg, G. E., & Senger, R. K. (1985). Automatic generation of flow nets with conventional groundwater modeling algorithms. *Ground Water*, 23, 336– 344.

Garashchuk, S. (2010). Quantum trajectory dynamics in imaginary time with the momentum-dependent quantum potential. *Journal of Chemical Physics*, 132( 014112). https://doi.org/10.1063/1.3289728

Garashchuk, S., Mazzuca, J., & Vazhappilly, T. (2011). Efficient quantum trajectory representation of wavefunctions evolving in imaginary time. *Journal of Chemical Physics*, 135, 034104. https://doi.org/10.1063/1.3610165

Garashchuk, S., & Vazhappilly, T. (2010). Multidimensional quantum trajectory dynamics in imaginary time with approximate quantum potential. *Journal of Physical Chemistry*, 114, 20,595– 20,602. https://doi.org/10.1021/jp1050244

Gelhar, L. W., & Axness, C. L. (1983). Three-dimensional stochastic analysis of macrodispersion in aquifers. *Water Resources Research*, 19, 161– 180.

Gelhar, L. W., Gutjahr, A. L., & Naff, R. L. (1979). Stochastic analysis of macrodispersion in a stratified aquifer. *Water Resources Research*, 15, 1387–1397.

Goldfarb, Y., Degani, I., & Tannor, D. J. (2006). Bohmian mechanics with complex action: A new trajectory-based formulation for quantum mechanics. *Journal of Chemical Physics*, 125( 231103), 1– 4.

Gu, B., & Garashchuk, S. (2016). Quantum dynamics with Gaussian bases defined by quantum trajectories. *Journal of Physical Chemistry*, 120, 3023–3031. https://doi.org/10.1021/acs.jpca.5b10029

Guerrero, J. S. P., & Skaggs, T. H. (2010). Analytical solution for one-dimensional advection-diffusion transport with distance-dependent coefficients. *Journal of Hydrology*, 390, 57– 65.

Harvey, C. F., & Gorelick, S. M. (1995). Mapping hydraulic conductivity: Sequential conditioning with measurements of solute arrival time, hydraulic head, and local conductivity. *Water Resources Research*, 31, 1615– 1626.

Herrera, P. A., Massabo, M., & Beckie, R. D. (2009). A meshless method to simulate solute transport in heterogeneous porous media. *Advances in Water Resources*, 32, 413– 429.

Herrera, P. A., Valocchi, A. J., & Beckie, R. D. (2010). A multidimensional streamline-based method to simulate reactive solute transport in heterogeneous porous media. *Advances in Water Resources*, 33, 711– 727.

Hewett, T. A., & Behrens, R. A. (1991). Scaling laws in reservoir simulation and their use in hybrid finite difference/streamtube approach to simulate the effects of permeability heterogeneity. In L. W. Lake, H. B. Carroll, & T. C. Wesson (Eds.), *Reservoir Characterization II* (pp. 402– 441). San Diego, CA: Academic Press.

Higgins, R. V., & Leighton, A. J. (1962). A computer methods to calculate two-phase flow in any irregularly bounded porous medium. *Journal of Petroleum Technology*, 14, 679– 683.

Hornung, U. (1997). *Homogenization and porous media interdisciplinary applied mathematics* (Vol. 6). Berlin: Springer-Verlag. https://doi.org/10.1007/978-1-4612-1920-0

Hudson, H. M., & Larkin, R. S. (1994). Ordered subsets of projection data. *IEEE Transactions on Medical Imaging*, 13, 601– 609.

Javandel, I., Doughty, C., & Tsang, C. F. (1984). *Groundwater transport: Handbook of models*. Washington, DC: American Geophysical Union Monograph.

Knessl, C., & Keller, J. B. (1997). Advection-diffusion past a strip. II. Oblique incidence. *Journal of Mathematical Physics*, 38, 267– 282.

Koch, D. L., & Brady, J. F. (1985). Dispersion in fixed beds. *Journal of Fluid Mechanics*, 154, 399– 427.

Koch, D. L., & Brady, J. F. (1987). The symmetry properties of the effective diffusivity tensor in anisotropic porous media. *Physics of Fluids*, 30, 642– 650.

Konikow, L. F., & Bredehoft, J. D. (1978). Computer model of two-dimensional solute transport and dispersion in ground water. *U. S. Geological Survey Water Resources Investigation*, 7, 50– 85.

Lichtner, P. C., Kelkar, S., & Robinson, B. (2002). New form of dispersion tensor for axisymmetric porous media with implementation in particle tracking. *Water Resources Research*, 38( 8), 21– 1/21-16. https://doi.org/10.1029/2000WR000100

Liu, Y., & Kitanidis, P. K. (2013). A mathematical and computational study of the dispersivity tensor in anisotropic media. *Advances in Water Resources*, 62, 303– 316.

Liu, J., & Makri, N. (2006). Bohm's formulation in imaginary time: Estimation of energy eigenvalues. *Molecular Physics*, 103, 6– 8. https://doi.org/10.1080/00268970512331339387

Mei, C. C. (1992). Method of homogenization applied to dispersion in porous media. *Transport in Porous Media*, 9, 261.

Menke, W. (1989). *Geophysical data analysis: Discrete inverse theory*. San Diego, CA: Academic Press.

Moridis, G. J. (2002). Semianalytical solutions of radioactive or reactive solute transport in a variably fractured layered media. *Water Resources Research*, 38( 12), 46– 1/46-24.

Nelson, R. W. (1978). Evaluating the environmental consequences of groundwater contamination: An overview of contaminant arrival distributions as general evaluation requirements. *Water Resources Research*, 14, 409–415.

Nikolaevskii, V. N. (1959). Konvektivnaya diffusiya v poristykh sredakh. *Prikladmaya Matematika i Mekhanika*, 23( 6), 1042– 1050.

Obi, E.-O., & Blunt, M. J. (2004). Streamline-based simulation of advective-dispersive solute transport. *Advances in Water Resources*, 27, 913– 924.

Oldenburg, C. M., & Pruess, K. (1993). A two-dimensional dispersion module for the TOUGH2 simulator (LBL Report 32505). Berkeley, CA: Lawrence Berkeley Laboratory.

Oldenburg, C. M., & Pruess, K. (1994). Numerical simulation of coupled flow and transport with TOUGH2: A verification study (LBL Report 35273). Berkeley, CA: Lawrence Berkeley Laboratory.

Oldenburg, C. M., & Pruess, K. (1995). Dispersive transport dynamics in a strongly coupled groundwater-brine flow system. *Water Resources Research*, 31, 289– 302.

Oldenburg, C. M., & Pruess, K. (1996). Mixing with first-order decay in variable-velocity porous media flow. *Transport in Porous Media*, 22, 161–180.

Oldenburg, C. M., & Pruess, K. (1998). Higher-order differencing for phase-front propagation in geothermal systems. In *Proceedings of the Twenty-Third Workshop on Geothermal Reservoir Engineering* (pp. SGP– TR-158). Stanford, CA.

Onsager, L. (1931a). Reciprocal relations in irreversible processes-I. *Physical Review*, 37, 405– 426.

Onsager, L. (1931b). Reciprocal relations in irreversible processes-II. *Physical Review*, 38, 2265– 2279.

Park, E., & Zhan, H. (2001). Analytical solutions of contaminant transport from finite one-, two-, and three-dimensional sources in a finite-thickness aquifer. *Journal of Contaminant Hydrology*, 53, 41– 61.

Press, W. H., Teukolsky, S. A., Vetterling, W. T., & Flannery, B. P. (1999). *Numerical recipes*. Cambridge: Cambridge University Press.

Prickett, T. A., Naymik, T. G., & Lonnquist, C. G. (1981). *A "random-walk" solute transport model for selected groundwater quality evaluations, Bulletin of the Ill State Water Survey* (Vol. 65). Champaign, IL: Illinois State Water Survey.

Pride, S. R., Vasco, D. W., Flekkoy, E. G., & Holtzman, R. (2017). Dispersive transport and symmetry of the dispersion tensor in porous media. *Physical Review E*, 95, 043103.

Pruess, K., Oldenburg, C., & Moridis, G. (1999). TOUGH2 user's guide, Version 2.0 (*43134*). Berkeley: LBNL Report.

Rubinstein, J., & Mauri, R. (1986). Dispersion and convection in porous media. *SIAM Journal of Applied Mathematics*, 46, 1018.

Saffman, P. G. (1959). A theory of dispersion in porous media. *Journal of Fluid Mechanics*, 6, 321– 349.

Scheidegger, A. E. (1954). Statistical hydrodynamics in porous media. *Journal of Applied Physics*, 25, 894– 1001.

Scheidegger, A. E. (1961). General theory of dispersion in porous media. *Journal of Geophysical Research*, 66, 3273– 3278.

Schwartz, F. W. (1977). Macroscopic dispersion in porous media: The controlling factors. *Water Resources Research*, 13, 743– 752.

Shan, C., & Javandel, I. (1997). Analytical solutions for solute transport in a vertical aquifer section. *Journal of Contaminant Hydrology*, 27, 63– 82.

Slichter, C. S. (1905). Field measurements of the rate of movement of underground waters (140). Washington, DC: U.S. Geological Survey Water Supply Paper.

Smith, R. (1981). The early stages of contaminant dispersion in shear flows. *Journal of Fluid Mechanics*, 111, 107– 122.

Strack, O. D. L. (1984). Three-dimensional streamlines in Dupuit-Forchheimer models. *Water Resources Research*, 20, 812– 822.

Tartakovsky, A. M., Tartakovsky, D. M., & Meakin, P. (2008). Stochastic langevin model for flow and transport in porous media. *Physical Review Letters*, 101( 044502), 1– 4. https://doi.org/10.1103/PhysRevLett.101.044502

Taylor, G. I. (1953). Dispersion of soluble matter in solvent flowing through a tube. *Proceedings of the Royal Society A*, 219, 186– 197.

Tsoflias, P. G., & Becker, M. W. (2008). Ground-penetrating-radar response to fracture-fluid salinity: Why lower frequencies are favorable for resolving salinity changes. *Geophysics*, 73, J25– J30. https://doi.org/101190/1.2957893

van Genuchten, M., & Alves, W. J. (1982). Analytical solutions of the one-dimensional convective-dispersion solute transport equation. *U.S.D.A Technical Bulletin*, 1661, 1– 151.

Vasco, D. W. (2018). An extended trajectory mechanics approach for calculating the path of a pressure transient: Derivation and illustration. *Water Resources Research*, 54, 1– 19. https://doi.org/10.1002/2017WR021360

Vasco, D. W., Bakulin, A., Baek, H., & Johnson, L. R. (2015). Reservoir characterization based upon the onset of time-lapse amplitude changes. *Geophysics*, 80, M1– M14. https://doi.org/10.1190/GO2014-0076.1

Vasco, D. W., Daley, T. M., & Bakulin, A. (2014). Utilizing the onset of time-lapse changes: A robust basis for reservoir monitoring and characterization. *Geophysical Journal International*, 197, 542– 556. https://doi.org/10.1093/gji/ggt526

Vasco, D. W., & Datta-Gupta, A. (1999). Asymptotic solutions for solute transport: A formalism for tracer tomography. *Water Resources Research*, 35, 1– 16.

Vasco, D. W., & Datta-Gupta, A. (2016). *Subsurface fluid flow and imaging*. Cambridge: Cambridge University Press.

Vasco, D. W., & Finsterle, S. (2004). Numerical trajectory calculations for the efficient inversion of transient flow and tracer observations. *Water Resources Research,* 40, W01507. https://doi.org/10.1029/2003WR002362

Vasco, D. W., Pride, S. R., & Commer, M. (2016). Trajecto ry-based modeling of fluid transport in a medium with smoothly varying heterogeneity. *Water Resources Research*, 52, 2618– 2646. https://doi.org/10.1002/2015WR017646

Wyatt, R. E. (2005). *Quantum dynamics with trajectories*. New York: Springer.

Yabusaki, S. B., Steefel, C. I., & Wood, B. D. (1998). Multidimensional, multicomponent, subsurface reactive transport in nonuniform velocity fields: Code verification using an advective reactive streamtube approach. *Journal of Contaminant Hydrology*, 30, 299– 331.

Yates, S. R. (1990). An analytical solution for one-dimensional transport in heterogeneous porous media. *Water Resources Research*, 26, 2331– 2338.

Zahasky, C., & Benson, S. M. (2018). Micro-positron emission tomography for measuring sub-core single and multiphase transport parameters in porous media. *Advances in Water Resources*, 115, 1– 16. https://doi.org/10.1016/j.advwatres.2018.03.002

Zheng, C., & Bennett, G. D. (1995). *Applied contaminant transport modeling: Theory and practice*. New York: Int. Thomson.